Surface & Coatings Technology 358 (2019) 467–480

Contents lists available at ScienceDirect

Surface & Coatings Technology

journal homepage: www.elsevier.com/locate/surfcoat

Phase interaction induced texture in a plasma sprayed-remelted NiCrBSi coating during solidification: An electron backscatter diffraction study

Liang-Yu Chen[a,b,c], Tianxiang Xu[a], Haiyang Wang[a], Peng Sang[c], Sheng Lu[a,*], Ze-Xin Wang[a], Shujin Chen[a], Lai-Chang Zhang[b,*]

[a] School of Materials Science and Engineering, Jiangsu University of Science and Technology, Zhenjiang, Jiangsu 212003, China
[b] School of Engineering, Edith Cowan University, 270 Joondalup Drive, Joondalup, Perth, WA 6027, Australia
[c] School of Science, Jiangsu University of Science and Technology, Zhenjiang, Jiangsu 212003, China

ARTICLE INFO

Keywords:
NiCrBSi
Coating
Spraying
Solidification
Texture
Phase interaction

ABSTRACT

Although considerable endeavors have been dedicated to investigate the microstructures of the remelting-enhanced NiCrBSi coatings, the textures in the remelted coatings, which may result in property anisotropy, are rarely studied. In this work, the recrystallized fractions, grain orientations and interphase boundaries for Ni, Ni_3B and CrB in a plasma sprayed-remelted NiCrBSi coating were investigated by electron backscatter diffraction. The results demonstrate that the texture is induced by phase interaction during solidification. Cooling from the liquid, the firstly formed Ni grains possess a cube fiber texture of {001}⟨001⟩. The successively formed Ni_3B colonies are randomly oriented and keep specific orientation relationships with the surrounding Ni grains, resulting in formation of some weak texture components of Ni. The finally formed CrB grains have a considerably high frequency (40.8%) of lattice correlation boundary of $(002)_{Ni}//(040)_{CrB}$, but no specific orientation relationships with Ni_3B grains. Hence, the interaction of Ni and CrB grains leads to the formation of more texture components of Ni. As such, the phase interaction induced texture forms in the remelted NiCrBSi coating. This work would give an insight into the anisotropy in the remelted NiCrBSi coatings and provide a theoretical basis of further optimizing the remelting process technologies.

1. Introduction

Nickel (Ni) and Ni-based alloy coatings have been widely used in many applications due to their high wear and corrosion resistance [1–7]. Among the coatings, NiCrBSi coatings are frequently used for engines, piston rods and boilers [1,2,8,9]. Traditionally, NiCrBSi coatings are synthesized by thermal spraying technologies, such as atmospheric plasma spraying (APS) [10], flame spraying [11] or high velocity oxygen fuel spraying (HVOF) [12]. As-sprayed NiCrBSi coatings possess a complex microstructure, primarily composed of Ni, Ni_3B, CrB and a small amount of other compounds depending on the specific compositions of feedstock [8,13–15]. Thermal spraying technologies provide a solution to protect the substrates; however, lamellar boundaries, pores and unmelted particles are often found in NiCrBSi coatings. These flaws degrade both the wear resistance and corrosion resistance properties of NiCrBSi coatings [16,17]. Therefore, post-processing technologies have been developed to enhance the properties of the as-sprayed NiCrBSi coatings.

Among the post-processing technologies, the remelting process is commonly used, which melts the coatings using a heat source and subsequently cools them at different cooling rates, depending on the post-processing method [16,18–20]. In general, the properties (i.e. corrosion and wear resistance) of the as-sprayed coatings can be significantly improved by remelting [16,18,21]. Therefore, considerable efforts have been made to investigate the microstructural evolution of the NiCrBSi coatings after spraying and remelting. Microstructural characterization indicates that the remelted NiCrBSi coatings have larger grain sizes than the as-sprayed NiCrBSi ones [22,23]. Meanwhile, the pores and lamellar boundaries in the remelted NiCrBSi are eliminated [16,19]. These previous works pointed out that the enhancements of the wear resistance and corrosion resistance properties of the NiCrBSi coatings are mainly attributed to the elimination of pores and lamellar boundaries, thereby increasing the inner cohesion in the remelted NiCrBSi coatings [16,18–20,24].

So far, the majority of investigations on the remelted NiCrBSi coating are concentrated on their phase constituents, morphologies and properties. Rare literature focuses on the textures of the remelted NiCrBSi coatings. It has been reported that the properties of the alloys

* Corresponding authors.
E-mail addresses: lusheng_ktz@just.edu.cn (S. Lu), l.zhang@ecu.edu.au, lczhangimr@gmail.com (L.-C. Zhang).

https://doi.org/10.1016/j.surfcoat.2018.11.019
Received 2 September 2018; Received in revised form 21 October 2018; Accepted 9 November 2018
Available online 22 November 2018
0257-8972/

Table 1
Plasma spraying and remelting parameters selected for depositing NiCrBSi coating.

Parameters	Spraying	Remelting
Voltage (V)	60	60
Current (A)	500	500
Powder feed rate (g/min)	17	–
Spray step (mm)	3	3
Gun traverse rate (mm/s)	100	10
Main gas Ar (slpm)	254	254
Secondary gas N_2 (slpm)	58	58
Feed gas Ar (slpm)	127	127
Spray distance (mm)	80	50
the number of spray or remelt	6	3

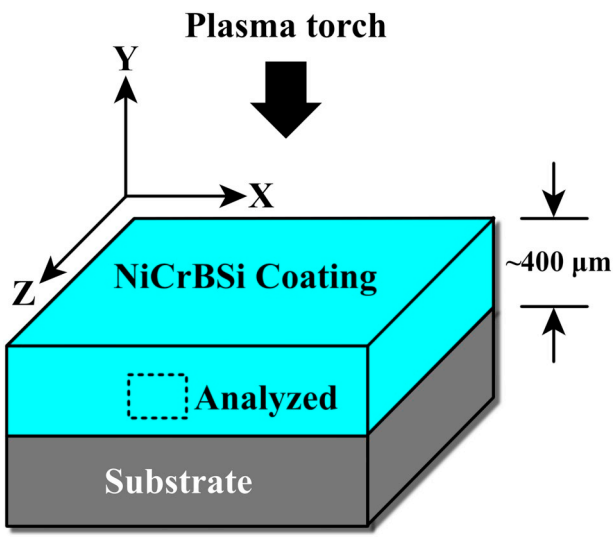

Fig. 1. Schematic interpretation of the coordinate axes of the remelted NiCrBSi coating sample in EBSD characterization.

Table 2
Crystallographic parameters of Ni, Ni_3B and CrB used in this work and the values of the average misorientation angle distribution (MAD) obtained from EBSD analysis.

Phase	Lattice parameters (nm)			Structure	Space group	Average MAD
	a	b	c			
Ni	0.3535	0.3535	0.3535	Face-centered cubic	Fm3m	0.18
Ni_3B	0.5211	0.6620	0.4396	Orthorhombic	Pnma	0.25
CrB	0.2969	0.7858	0.2932	Orthorhombic	Cmcm	0.41

can be substantially influenced their textures [25–29]. For example, the Cu-Y_2O_3 composite coatings with {111} texture possess higher hardness [27]. Narin et al. [26] found that the corrosion resistance of electrogalvanized chromate coatings could be enhanced by tailoring the {100} crystallographic planes. Hence, it is believed that similar scenario might occur in the remelted NiCrBSi coatings. As the NiCrBSi coatings possess multiphase microstructures, different phases would form from the melt successively at different temperature during solidification [30]. In such a case, the interaction of the grain orientations between the formed phase and the successively formed phase would take place during solidification [31]. Some phases in the NiCrBSi coatings with low symmetries, such as Ni_3B and CrB (orthorhombic structure), have strong anisotropies, which may potentially influence the wear resistance and/or corrosion resistance of the remelted NiCrBSi coatings. Hence, the crystallographic characteristics (i.e. textures and interphase

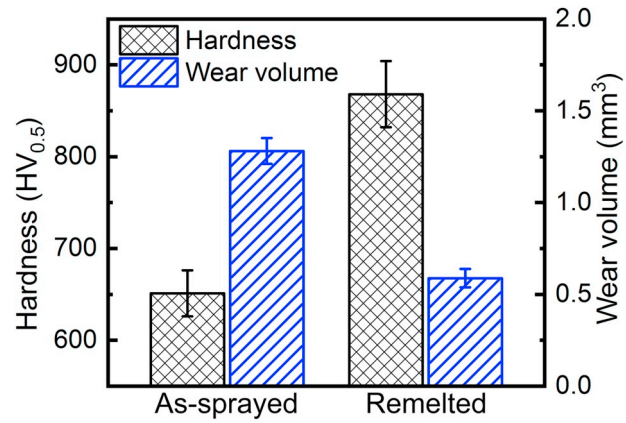

Fig. 2. Hardness and wear volume of the as-sprayed and remelted NiCrBSi coatings.

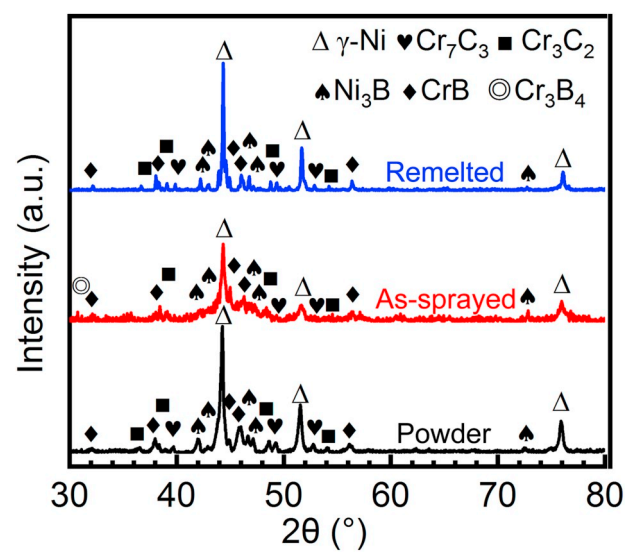

Fig. 3. XRD patterns of the raw powder, the as-sprayed and remelted NiCrBSi coatings.

boundaries) of alloys are being commonly interested [31–35]. It is well known that electron backscatter diffraction (EBSD) technique has been extensively used to obtain statistical data of the crystallographic characteristics, such as phase identifications, grain orientations and boundary misorientations [31,36–38]. Unfortunately, there are rare studies on the crystallographic characteristics of the remelted NiCrBSi coatings. As mentioned above, NiCrBSi coatings have multiphase microstructures and the phases would interact with each other during solidification, it is therefore highly important to deeply investigate the crystallographic characteristics of the remelted NiCrBSi coatings, which would shed light on the anisotropy in the remelted NiCrBSi coatings and offer a theoretical basis of further optimizing the remelting process methods.

In our previous study, the microstructures of the as-sprayed and heat-treated NiCrBSi coatings as well as their performance are investigated in detail [3]. In comparison to the conventional manual-remelting method, we develop a new method of plasma re-heat treatment to remelt the as-sprayed NiCrBSi coating in this work. The outcome shows that the remelted NiCrBSi coating has the comparable hardness and wear resistance with the results reported by other methods in previous literature [4,8,39]. Therefore, regarding a further improvement of the properties, more attention should be paid to the study of the microstructure of the remelted NiCrBSi coating, especially the phase interaction induced texture. Ni-Cr-B ternary alloy has been used as filler

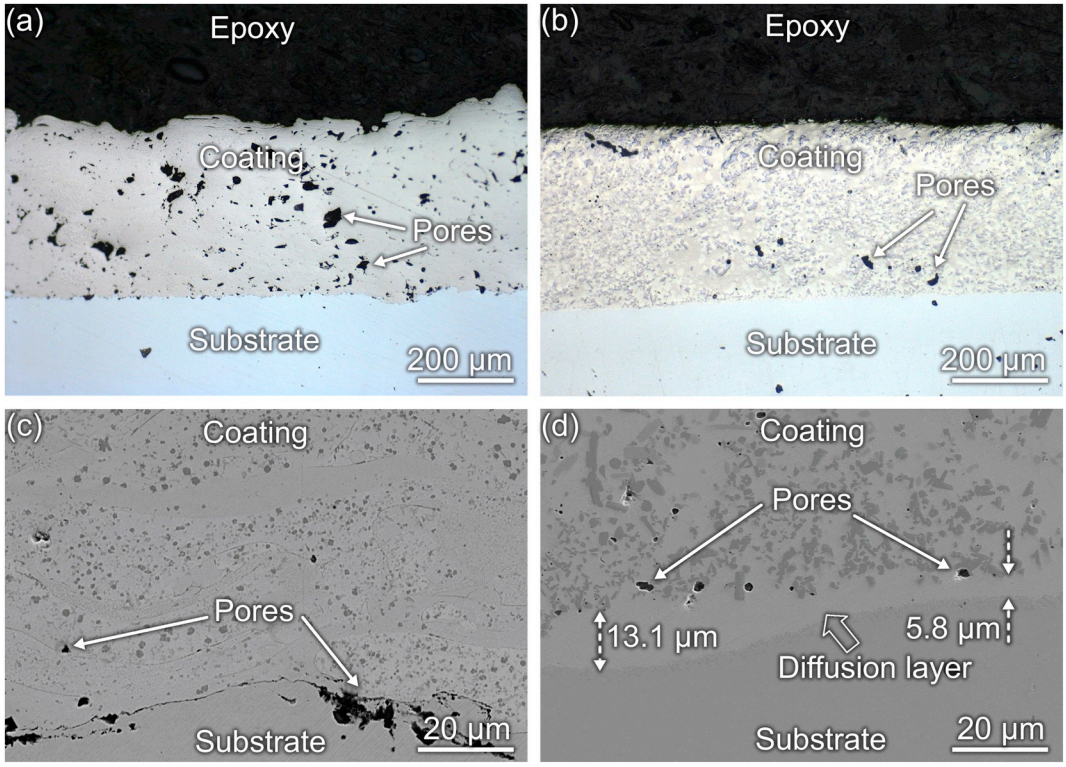

Fig. 4. Cross-sectional microstructures of the coatings: optical microscopy images for (a) as-sprayed and (b) remelted NiCrBSi coatings and scanning electrons microscopy image for (c) as-sprayed and (d) remelted NiCrBSi coatings.

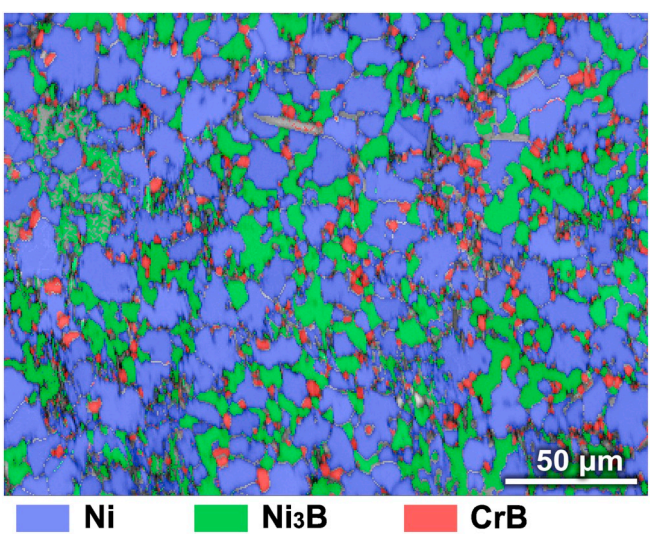

Fig. 5. Grain color map of the remelted NiCrBSi coating.

materials for several decades [40]. During the development of the alloy, many other elements are added in this system in order to improve the properties of the Ni-Cr-B ternary alloy [41–43]. Although the chemical compositions of developed alloy are different, all of them are based on the Ni-Cr-B ternary system. Three phases of Ni, Ni_3B and CrB can be found almost in all Ni-Cr-B ternary alloy and its derivatives. Meanwhile, although Cr-C compounds were found in our previous work [3], the total volume fraction of Cr-C compounds is lower than 10%. Therefore, considering the general applicability of this work, choosing Ni, Ni_3B and CrB for analysis may be a better choice. As such, EBSD technique is adopted in this work to study the recrystallized fractions and grain orientations for Ni, Ni_3B and CrB and the interphase boundaries between them in a NiCrBSi coating prepared by plasma spraying followed by remelting. The EBSD results can provide insight into the formation of phase interaction induced texture in the remelted NiCrBSi coating during solidification.

2. Experimental

2.1. Coating preparation

The as-sprayed coating was manufactured by gas atomized NiCrBSi feedstock using a SG-100 plasma-spraying torch (Praxair, USA). An Ar gas shrouded plasma spray torch was used to reduce the particle oxidation during the in-flight process. The NiCrBSi feedstock was produced in BGRIMM Advanced Materials Science and Technology Co., Ltd. The particle size of the feedstock was between 45 μm and 109 μm. The feedstock contained 16.2% Cr, 3.0% B, 4.5% Si 0.6% C, 5.3% Fe and with Ni as balance (all in wt%). The NiCrBSi coating was deposited on a 2Cr13 stainless steel substrate (40 mm × 40 mm × 10 mm) which was cleaned by acetone to eliminate oil contamination and treated by grit blasting. The remelting process with different parameters was conducted by using SG-100 plasma-spraying torch to heat the as-sprayed coating samples but no feedstocks were provided. As the surfaces of the substrates are covered by the coatings, the temperature of the substrate was recorded on its back by an infrared thermometer. During spraying or remelting, the temperature of the substrate ranged from 200–271 °C to 314–592 °C, respectively. During the remelting process, the temperature of the coating was greater than 1500 °C. After remelting, the remelted coating was cooled in air and about 400 μm in thickness. During the whole process (including spraying and remelting), the samples were fixed on a shelf. The detailed plasma spraying and remelting parameters selected are listed in Table 1. After remelting, a very thin diffusion/mixing layer is formed between the substrate and coating, which is the same as the phenomena reported in the literature [5,11]. Therefore, this thin diffusion/mixing layer would not affect the chemistry of the rest of the coating.

Table 3
Recrystallized, substructured and deformed fractions[a] (vol%) for Ni, Ni_3B and CrB in the NiCrBSi coating.

Phase	Recrystallized	Substructured	Deformed
Ni	93.6	5.8	0.6
Ni_3B	68.4	29.6	2.0
CrB	91.7	1.2	7.1

[a] The defining of a recrystallized, substructured or deformed grain is according to the internal average misorientation angle. If the grain consists of no subgrains and its internal average misorientation angle is below 1°, this grain is recrystallized. If the grain consists of subgrains and its internal average misorientation angle is below 1°, this grain is substructured. The remaining grains were classified as deformed [47].

2.2. Characterization

For the microstructure observations, the coating samples were mounted in conductive resin, mechanically ground with SiC up to 2000 grits and polished to a mirror surface. A field emission gun scanning electron microscope (SEM, Zeiss Sigma HD, German) equipped with an energy dispersive spectrometer (EDS) and an optical microscope (OM, Zeiss Axioskop2-MAT, German) was used to observe the cross-sectional microstructures of the coatings. The porosity was obtained by the Software of Image J2X. For the EBSD observations, the polished coating sample was vibratory polished using colloidal silica for 4 h to remove the deformed surface layer. The EBSD examination was conducted on the cross-sections of the remelted coating using an AZtec HKL Max system fitted on the SEM under the acceleration voltage of 20 kV with the step size of 600 nm. The coordinate axes of the remelted coating sample are shown in Fig. 1, where direction Y is perpendicular to the sample surface and directions X and Z are parallel to the sample surface. Therefore, the analyzed plane was the X-Y plane.

The EBSD data were analyzed by the Channel 5 software. Since selecting more than three phases during EBSD examination may lead to incorrect indexing, only three phases of Ni, Ni_3B and CrB were chosen for examination because these three phases are well known in the NiCrBSi coating [8,40]. After refining 6.9% EBSD data for the reduction of noisy points, the total indexing rate is 89.9%. In general, high angle grain boundary and low angle grain boundary are defined as 15° (10° in some literature) and 1° misorientations between two neighboring grains [44–46]. Therefore, the grain boundary angle conditions are chosen as 15° and 1° to illustrate the grains and subgrains, respectively. As a result, for each phase, the grain was classified as deformed if the internal average misorientation angle was greater than 1° within this grain, whereas the grain was classified as substructured if the grain consisted of subgrains but the internal average misorientation angle was below 1° within this grain, and the remaining grains were classified as recrystallized [47]. The crystallographic parameters of Ni, Ni_3B and CrB used in this work are listed in Table 2, which were extracted from JCPDS#65-0380, JCPDS#48-1223 to JCPDS#65-6696. For orthorhombic structure, the analytic relationships between orientation g $\{\varphi_1, \phi, \varphi_2\}$ and texture components $\{hkl\}\langle uvw\rangle$ could be expressed according to the Ref. [48] using the equations below:

$$h{:}\ k{:}\ l = a\sin\phi\sin\varphi_2{:}\ b\sin\phi\cos\varphi_2{:}\ c\ \cos\phi \tag{1}$$

and

$$u{:}\ v{:}\ w = \frac{(\cos\varphi_1\cos\varphi_2 - \sin\varphi_1\cos\phi\sin\varphi_2)}{a} : \frac{(-\cos\varphi_1\sin\varphi_2 - \sin\varphi_1\cos\phi\cos\varphi_2)}{b} : \frac{\sin\varphi_1\sin\phi}{c} \tag{2}$$

where the h, k and l are the indices of crystal faces, u, v and w are the indices of crystallographic orientations, the φ_1, ϕ and φ_2 are the three Euler angles in the Bunge system. Herein, the $\{hkl\}$ planes of the grains lie perpendicular to the direction Z of the remelted coating sample, whereas their $\langle uvw\rangle$ directions are parallel to the direction X of the remelted coating sample. For face-centered cubic (FCC) structure, the lattice parameter a = b = c.

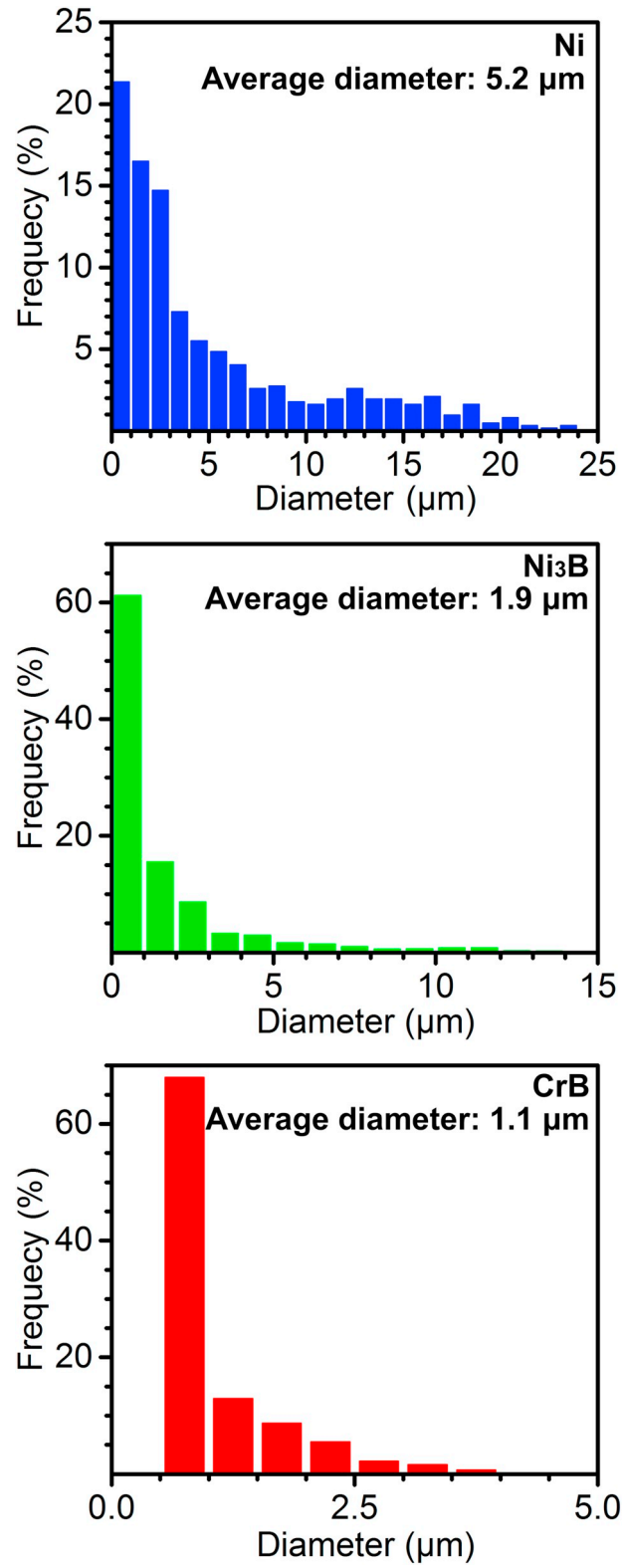

Fig. 6. Size distributions of the Ni, Ni_3B and CrB grains in the remelted NiCrBSi coating.

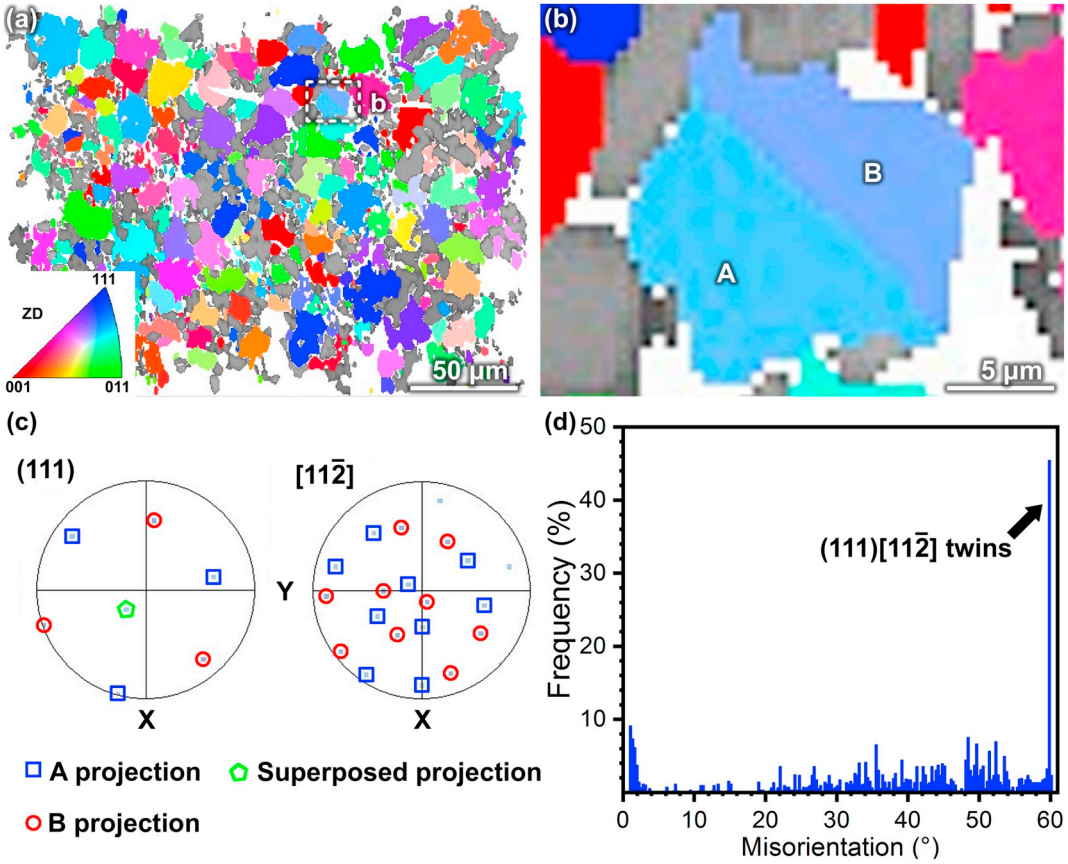

Fig. 7. EBSD results of the remelted NiCrBSi coating: (a) inverse pole figure map for Ni grains, (b) magnified image of the dash region b in (a), (c) the (111) and [11$\bar{2}$] pole figures of A and B parts marked in (b), (d) misorientation angle distribution histogram of the neighboring Ni grains.

2.3. X-ray diffraction

X-ray diffraction (XRD) was conducted on a D8 Advance A25X diffractometer to analyze the phase constituents of the raw powder and the remelted coatings. The scanning range is from 30° to 80°, the scanning speed is 2 °/min and the scanning step is 0.02°. The XRD patterns were analyzed by the Jade 6.5 software.

2.4. Hardness and wear volume

The Vickers hardness was carried out on the X-Y planes of the as-sprayed and remelted NiCrBSi coatings (KB30S, German). Before the tests, the coatings were ground and polished. The indentation load was 5 N with the dwell time of 15 s. The reported hardness of each sample was averaged from ten tested points. The pin-on-disc tribological tests were carried out on the X-Z of the polished sample without lubrication in air (Bruker UMT-2, German) according to ASTM G99. The testing parameters were as follows: 4 mm diameter wear track; 20 N load; ZrO_2, 5 mm diameter counterpart; 50 rpm slide speed; 1800 s testing time. Three different measurements were performed for each sample. The average wear volumes were measured by 3D confocal laser-microscopy (Olympus OLS4000) at 5 different places on the wear tracks.

3. Results

3.1. Hardness and wear volume

Fig. 2 exhibits the hardness and wear volume of the as-sprayed and remelted NiCrBSi coatings. Obviously, the hardness of the remelted coating (868 $HV_{0.5}$) is much higher than that of the as-sprayed coating (651 $HV_{0.5}$). Correspondingly, the wear volume of the remelted coating (0.588 mm^3) is also much less than that of the as-sprayed coating (1.281 mm^3). Therefore, it seems that the remelted NiCrBSi coating prepared using plasma torch has comparable hardness and wear resistance with the remelted NiCrBSi coatings produced by other methods in the literature [4,8,39], illustrating the feasibility of this remelting method. However, a deep investigation of the microstructure for the remelted NiCrBSi coating, especially crystallographic characteristics, is rarely addressed. Hence, a detailed characterization of the remelted NiCrBSi coating is carried out in terms of recrystallized fractions, grain orientations and interphase boundaries for Ni, Ni_3B and CrB in the following text.

3.2. Microstructural features

Fig. 3 reveals the XRD patterns of the raw powder, the as-sprayed and remelted coatings. It could be found that the raw powder mainly consists of γ-Ni, Ni_3B, CrB, Cr_7C_3 and Cr_3C_2. Due to the existence of C in the raw powder, Cr_3C_2 and Cr_7C_3 peaks are found in the corresponding XRD pattern. It is also reported that a small amount of Fe and Si would be in solid solution to form γ-Ni [30,49], thereby no Fe-based compounds and silicide are observed in the XRD pattern. Fe-based intermetallic phases have been rarely reported in previous research with respect to the NiCrBSi coatings with the same or similar compositions [1,22,50]. The phase constituents of the as-sprayed NiCrBSi coatings are the same as those of the raw powder, except for the presence of Cr_3B_4. Additionally, it is observed that a broad diffuse diffraction is apparent from 40° to 50°. In our previous work, such phenomena are attributed to the fast cooling rate of the deposition process, leading to the formation of the amorphous phase and metastable phase (i.e. Cr_3B_4) [3,51,52]. However, the amorphous phase and metastable phase are prone to disappear after heat treatment or cooling at a slow rate [3].

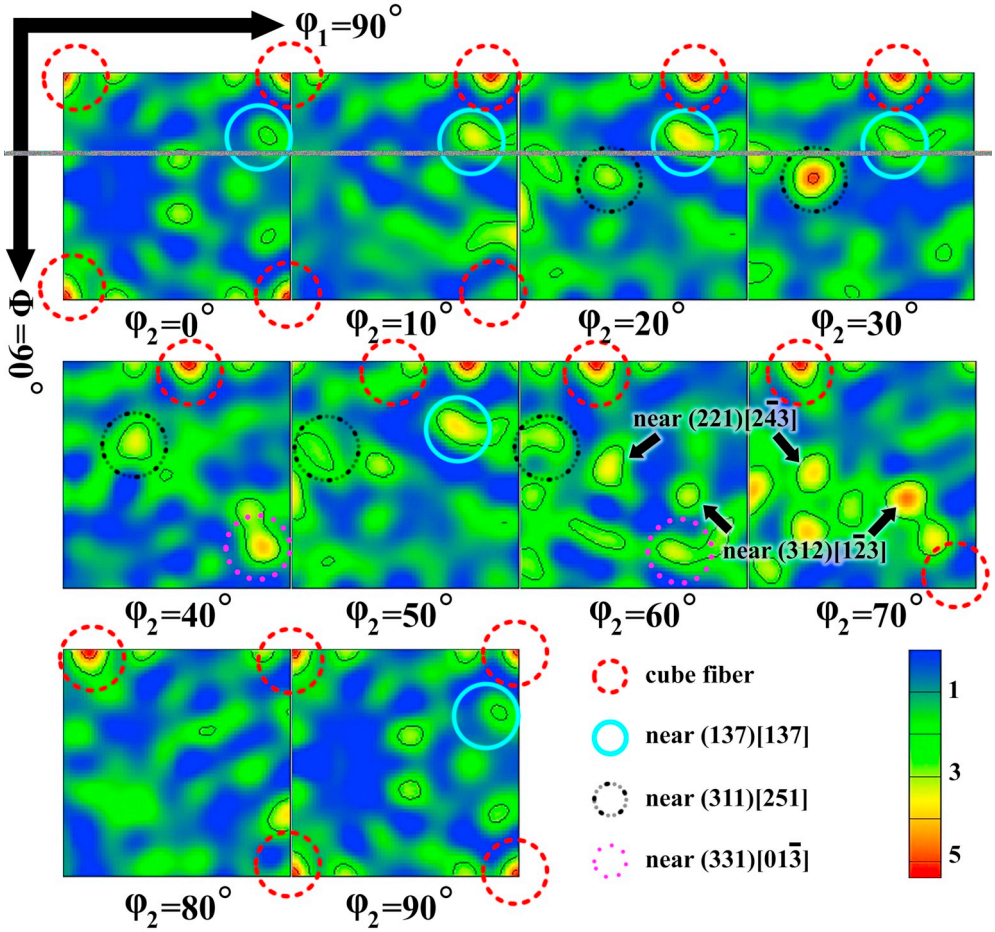

Fig. 8. Selected orientation distribution functions of the Ni grains in the NiCrBSi remelted coating.

Therefore, the phase of Cr_3B_4 disappears after remelting. The other phases in the remelted NiCrBSi coatings are the same as those in the raw powder. Compared with XRD pattern of the remelted NiCrBSi coating, the peaks on the XRD pattern of raw powder are slightly broadened. In previous reports, such broadening is also caused by the amorphous phase or nanocrystalline [51,53–56]. By contrast, the peaks on the XRD pattern of the remelted NiCrBSi coating become sharp, elucidating that the remelted NiCrBSi coating have a higher degree of crystallinity and greater grain size. As seen from Fig. 3, the peaks of Cr_7C_3 and Cr_3C_2 are substantially weak, specifying that the volume fractions of these two phases are significantly low in the remelted NiCrBSi coating, which is in line with the results in the literature [8,40]. Therefore, γ-Ni, Ni_3B, CrB phases are chosen in the EBSD analysis.

Fig. 4 shows the cross-sectional microstructures of the as-sprayed and remelted NiCrBSi coatings. As seen from Fig. 4a, a large number of pores are presented in the as-sprayed NiCrBSi coating. After remelting, the number of pores in the remelted NiCrBSi coating is significantly reduced since the NiCrBSi alloys possess appreciable fluidity and wettability (Fig. 4b) [15]. Calculated from at least ten OM images, the porosities of the as-sprayed and remelted NiCrBSi coatings are 2.72% ± 0.86% and 0.82% ± 0.17%, respectively. Fig. 4c reveals the coating/substrate interface of the as-sprayed NiCrBSi coating. The coating and the substrate are bonded with a mechanical engagement, accompanied by a large number of pores. Conversely, the coating/substrate interface of the remelted NiCrBSi coating becomes a metallurgical bonding (Fig. 4d). A diffusion layer with the thickness of 5.8–13.1 μm forms between the coating and the substrate, indicating that the heat affected depth is greater than the thickness of the coating. Such results demonstrate that the method developed in this work can produce a dense remelted NiCrBSi coating with comparable properties compared with those reported in the literature [8,40]. In order to better understand the crystallographic characteristics of the remelted NiCrBSi coating, systematical EBSD characterization is employed in the following work. Furthermore, the oxygen contents in the as-sprayed and remelted coatings were examined by EDS at ten different locations and the results show that the average oxygen contents of the as-sprayed coating are 1.07 ± 0.45 wt% and 1.16 ± 0.47 wt%, respectively. This result illustrates that the remelting process did not cause severe oxidation of the NiCrBSi coating, resulting from its self-fluxing nature [4].

Fig. 5 shows a grain color map of the remelted NiCrBSi coating where Ni, Ni_3B and CrB are indexed as blue, green and red colors, respectively. The volume fractions of Ni, Ni_3B and CrB are 59.6%, 24.6% and 5.7%, respectively. It could be seen that the Ni, Ni_3B and CrB grains are uniformly distributed in the remelted coating. Most Ni grains are equiaxed or nearly equiaxed. The Ni_3B grains are in a floret shape and surrounded with Ni grains. It is noted that the Ni_3B grains are primarily produced by the eutectic reaction in NiCrBSi coatings [9]. Such a morphology of Ni_3B grains is commonly observed in Ni-Ni_3B eutectic structure [8,9]. The CrB grains are in a very small size and most of them are embedded in or adjacent to the Ni grains. By comparison, not all CrB grains are adjacent to the Ni_3B grains. Furthermore, the recrystallized fraction associated with substructured and deformed fractions for Ni, Ni_3B and CrB are investigated and listed in Table 3. The Ni and CrB have very high recrystallized fractions of 93.6 vol% and 91.7 vol%, respectively. By contrast, the recrystallized fraction of Ni_3B is merely 68.4 vol%, while the Ni_3B has a relatively high substructured fraction of 29.6 vol%. As aforementioned, the substructured grains

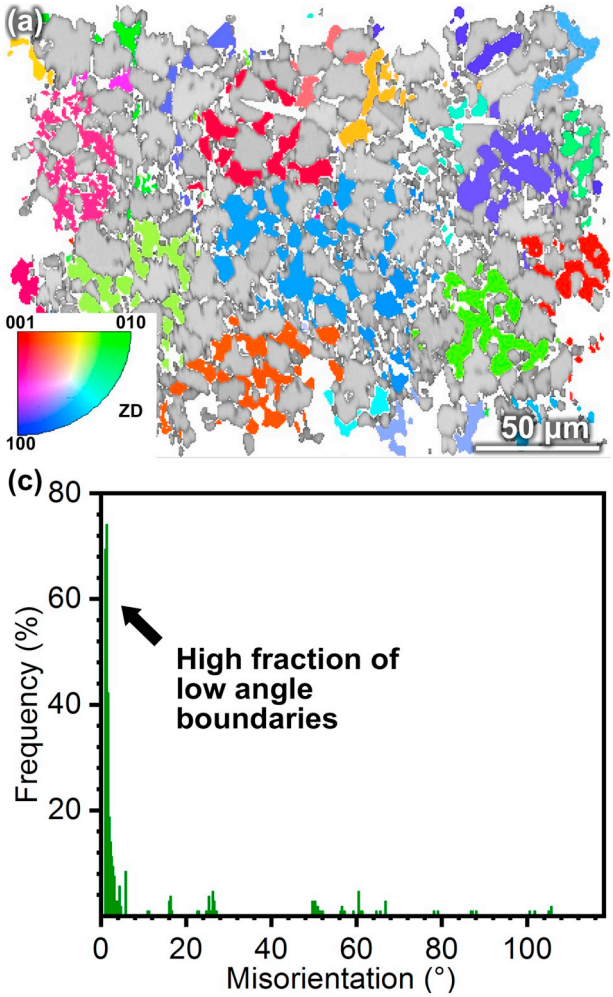

Fig. 9. EBSD results of the remelted NiCrBSi coating: (a) inverse pole figure map for Ni_3B grains, (b) misorientation angle distribution histogram of the neighboring Ni_3B grains.

consist of subgrains and the misorientations of these subgrains range from 1° to 15° [47]. It is known that internal misorientation within a grain always means lattice strains and defects [57]. Hence, one can conclude that the Ni_3B grains have relatively higher lattice strain and defect density than the Ni and CrB grains.

As the properties of many alloys are influenced by grain sizes [58,59], the further investigation of the Ni, Ni_3B and CrB grain sizes in the remelted NiCrBSi coating is exhibited in Fig. 6. The sizes of grains in the remelted coating are calculated in terms of the circle equivalent diameter [47]. The Ni grains range from 0.6 to 25 μm with the average diameter of 5.2 μm. The Ni_3B grains range from 0.6 to 12 μm and the average diameter is 1.6 μm, which is smaller than that of the Ni grains. CrB grains are quite small with 1.1 μm in average diameter. Although the average grain sizes of Ni, Ni_3B and CrB in the as-sprayed NiCrBSi coating are rarely reported, the average grain size of Ni in the Ni coatings prepared by plasma spraying (about 1 μm) [60] and by cold spraying (CS) (from 100 nm to 5 μm) [57] are much smaller than that in the remelted NiCrBSi coating in this work. Such a difference should be attributed to the relatively slow cooling rate of the solidification without any impact in the remelted NiCrBSi coating. Because the necessary time for the solidification of the molten particles is between 10^{-6} and 10^{-8} s during deposition by conventional APS technology [13], thereby the growth of the grains in APS-produced coatings is restricted due to the fast cooling rate [3]. For CS technology, high impact breaks up the grains in the CS-produced coatings, however, the temperature is not high enough to promote the growth of the grains [57]. By contrast, the remelted NiCrBSi coating was remelted at first and then cooled down in air at a relatively slow rate. The time for solidification and cooling is long enough to support the growth of the grains to some extent.

3.3. Grain orientations

To reduce the artificial results, the analysis of the grain orientations only considers the grains containing more than 9 pixels. This operation is the same for Ni, Ni_3B and CrB phases represented in the following. Fig. 7a shows the inverse pole figure (IPF) map for Ni grains in the remelted NiCrBSi coating, where the Ni grains in various orientations are indexed as different colors. By referring to the color scale, one can find that a large number of Ni grains have the {001} planes perpendicular to or approximately perpendicular to the direction Z of the sample. Fig. 7b is a magnified image of the dash rectangle region b in Fig. 7a, showing that a Ni grain is presented as two different colors (marked as A and B) with a straight boundary. By investigating the orientations of A and B parts, the (111) and $[11\bar{2}]$ pole figures reveal a symmetrical relationship between them, indicating the presence of the $(111)[11\bar{2}]$ twins in this Ni grain (Fig. 7c). Such a type of twins in Ni grains is widely observed in Ni-based alloys and has a lattice rotation by 60° [61]. $(111)[11\bar{2}]$ twins are always found in deformed and annealed Ni alloys [61,62], demonstrating that both stress and redistribution of dislocations on grain boundaries could induce $(111)[11\bar{2}]$ twins in Ni grains. Regardless of the formation reason, it is shown in Fig. 7d that the misorientation of the neighboring Ni grains basically exhibits a random distribution except for an evident peak around 60°, confirming the extensive existence of $(111)[11\bar{2}]$ twins in the Ni grains in the remelted NiCrBSi coating.

In order to give a textural analysis of the Ni grains in the remelted coating in detail, the orientation distribution functions (ODFs) are represented in Fig. 8. A very strong cube fiber of (001)[100] are observed as indicated by red dash cycles. Cube fiber texture component is always found in the as-cast and/or recrystallized Ni-based alloys [63,64]. In this work, the as-sprayed NiCrBSi coating was remelted by plasma torch, then cooled down in air. Such a process could be regarded as a solidification of NiCrBSi alloy at a relatively slow rate, which promotes the generation of cube fiber texture of the Ni grains in the remelted NiCrBSi coating. Besides cube fiber texture, three major texture components, close to the (137)[137], (311)[251] and $(331)[0\bar{1}3]$, could be found as indicated by light blue, black dash-dot, purple dot cycles in Fig. 8. These three texture components have lower intensities than the cube fiber, which is consistent with the results obtained from the IPF map for Ni grains in Fig. 7a. Furthermore, some other texture components with very weak intensities could be found, such as $(221)[2\bar{4}3]$ and $(312)[1\bar{2}3]$. The study of the texture reveals that most Ni grains are primarily cube-oriented, which should be ascribed to the preferential nucleation of the Ni grains during solidification [64].

Fig. 9a shows the IPF map for Ni_3B grains in the remelted NiCrBSi coating, representing the continuous Ni_3B colonies by the same color. However, the independent Ni_3B colonies reveal distinctive orientations (colors) and are varied one by one. The misorientation angle distribution histogram of neighboring Ni_3B grains is shown in Fig. 9b which represents that the fraction of low angle boundaries is more than 70%. Considering the discontinuity of most Ni_3B grains (Fig. 9a), therefore, it is reasonable speculated that such a high fraction of low angle boundaries is a result of the sub-grain boundaries in the Ni_3B grains. This deduction is consistent with the result of the relatively high substructured fraction in Table 3. Additionally, no specific misorientation among neighboring Ni_3B grains is observed. The ODFs of the Ni_3B grains in the remelted coating are shown in Fig. 10. Because of the lattice parameter $a \neq b \neq c$ in the orthorhombic structure of Ni_3B, the φ_2 ranges from 0 to 180° in the ODFs (the same for CrB, hereafter). As expect, the Ni_3B grains present very strong texture due to the limited

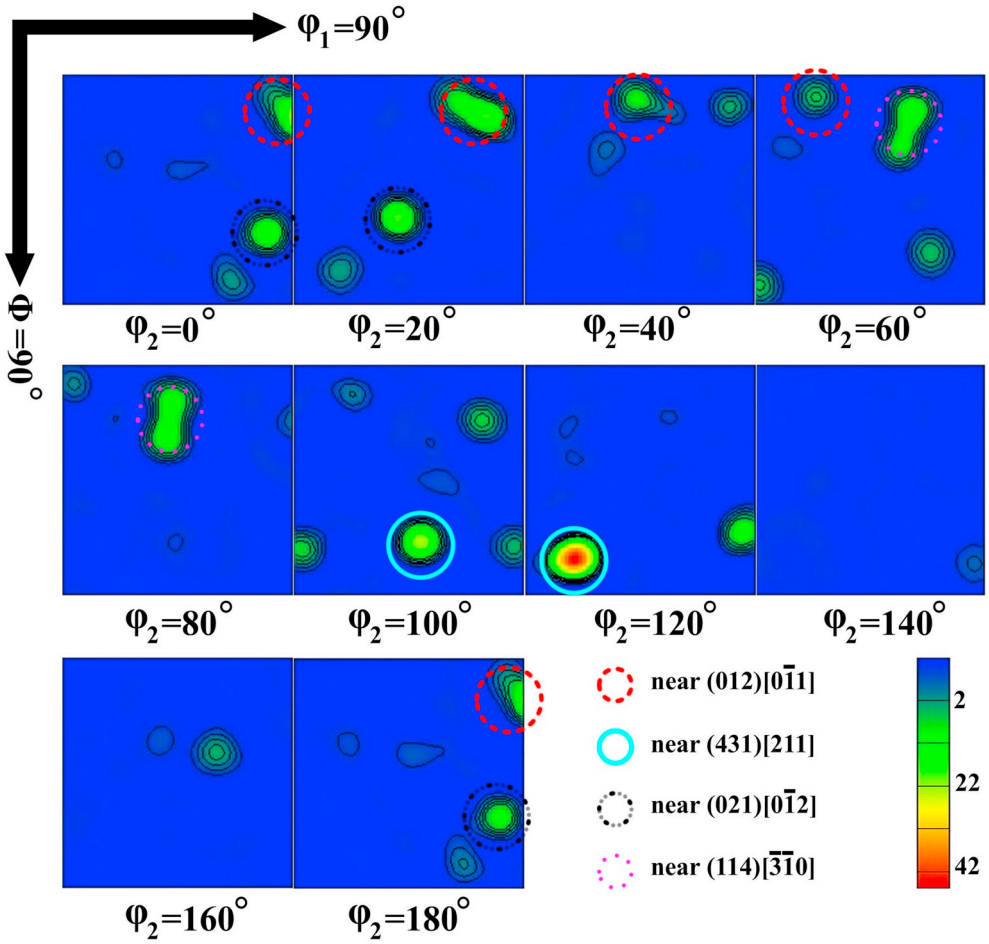

Fig. 10. Selected orientation distribution functions of the Ni_3B grains in the remelted NiCrBSi coating.

grains analyzed. Four major texture components of (012)[0$\bar{1}$1], (431)[211], (021)[0$\bar{1}$2] and (114)[$\bar{3}\bar{1}$0] are calculated from the ODFs. Apparently, the misorientation angles between texture components cover a wide range from several degrees to about 90°, indicating that the orientations of the Ni_3B grains are primarily random.

Fig. 11a shows the IPF map for CrB grains in the remelted NiCrBSi coating. It could be seen that majority of CrB grains display a green color, indicating that the (010) planes of these CrB grains are perpendicular to or nearly perpendicular to the direction Z of the sample. Fig. 11b is a magnified image of the dash rectangle region b in Fig. 11a. Similar to the Ni grain in Fig. 7b, it shows that a CrB grain is presented as two different colors (marked as E and F) with a straight boundary. In the view of (110) and [1$\bar{1}$0] pole figures, these two parts have a symmetrical relationship, signifying the presence of the (110)[1$\bar{1}$0] twins in this CrB grain (Fig. 11c). According to the lattice parameters of CrB phase, it could be calculated that the (110)[1$\bar{1}$0] twins have a lattice rotation by 41.4° along the (110) plane. As seen from the Fig. 11d, the misorientation of 40°–44° has a very high frequency among the neighboring CrB grains, which means that (110)[1$\bar{1}$0] twins are highly resided in the CrB grains.

Fig. 12 shows the ODFs of the CrB grains in the remelted NiCrBSi coating. It is interesting that the texture components are primarily located at about ϕ = 80–90° in each ODF section. The strongest texture component observed is close to ideal (010)[001] and (010)[101], within 10° deviation. This result is consistent with the observation in Fig. 11a. The angle between [001] and [101] directions in CrB grain is 45.4°, close to the misorientation angle of 41.4° in (110)[1$\bar{1}$0] type twins, indicating that such two orientations ((010)[001] and (010)[101]) represented in an individual ODF section may result from the highly resided twins in CrB grains. The other two major texture components are close to ideal (212)[$\bar{1}\bar{2}$2] and (212)[$\bar{3}\bar{1}$3], (170)[302] and (170)[203]. The angle between [$\bar{1}\bar{2}$2] and [$\bar{3}\bar{1}$3] directions in CrB grain is 36.8°, also approaching 41.4°. These findings may imply that the texture components presented in pairs in the ODF sections may be related to the highly resided twins in CrB grains.

3.4. Lattice correlation boundaries

Fig. 13 shows the lattice correlation boundaries between the adjacent Ni and Ni_3B grains and between the adjacent Ni and CrB grains, respectively. In this work, the lattice correlation boundary describes the interphase boundary with a specific orientation relationship of planes parallel between two phases. For instance, a type of lattice correlation boundary $(h_1k_1l_1)_{Ni}//(h_2k_2l_2)_{Ni_3B}$ means that the $(h_1k_1l_1)$ plane of Ni is parallel to the $(h_2k_2l_2)$ plane of Ni_3B between a couple of adjacent Ni and Ni_3B grains. As seen from Fig. 13a, four types of lattice correlation boundaries between Ni and Ni_3B grains, i.e. $(311)_{Ni}//(114)_{Ni_3B}$, $(311)_{Ni}//(241)_{Ni_3B}$, $(022)_{Ni}//(420)_{Ni_3B}$ and $(001)_{Ni}//(001)_{Ni_3B}$ within 5° tolerance, are exhibited by red, blue, green and purple lines, respectively. By comparing the IPF map of Ni_3B (Fig. 9a), two independent Ni_3B colonies (dark grains) are contained in the rectangles G and H in Fig. 13a. It can be seen that almost all green lines in the Fig. 13a are concentrated in the dash rectangle G, illustrating that the independent Ni_3B colony has a specific orientation relationship with the surrounding Ni grains. Moreover, the lattice correlation boundaries around the Ni_3B colony mainly represent red and blue colors in the dash rectangle H. Such a situation could be found elsewhere in Fig. 13a. By relating to the IPF map of Ni (Fig. 9a), it confirms again that the independent Ni_3B

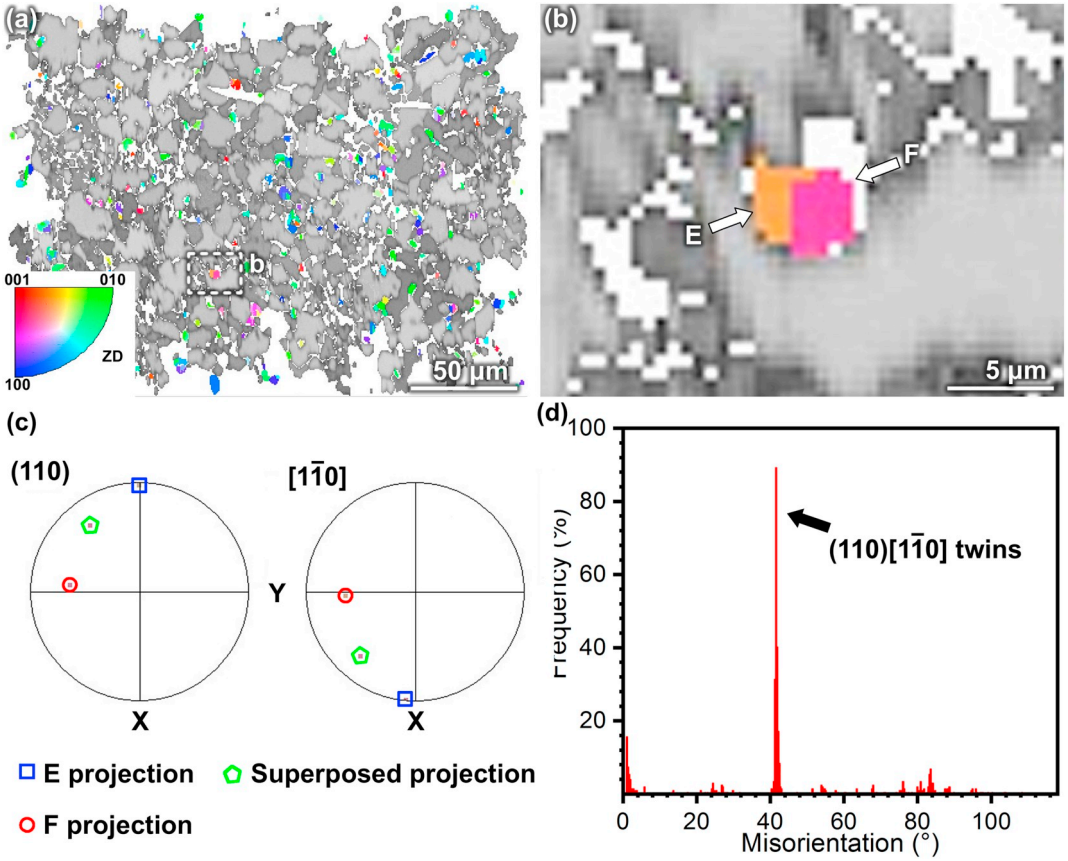

Fig. 11. EBSD results of the remelted NiCrBSi coating: (a) inverse pole figure map for CrB grains, (b) magnified image of the dash rectangle region b in (a), (c) the (110) and [1$\bar{1}$0] pole figures of E and F parts marked in (b), (d) misorientation angle distribution histogram of the neighboring Ni grains.

colony has the specific orientation relationships with the surrounding Ni grains even if the surrounding Ni grains have distinctive orientations. Table 4 summarizes the lattice mismatches between different couples of the low-index planes of Ni and Ni_3B and the corresponding frequencies of the lattice correlation boundaries. The frequency of the lattice correlation boundary is defined as the ratio of the length of a certain type lattice correlation boundary and the total length of the interphase boundary between the examined two phases. Ajao et al. [65] and Shapiro et al. [66] had suggested the orientation relationships of $(311)_{Ni}//(420)_{Ni_3B}$, $(111)_{Ni}//(130)_{Ni_3B}$, $(002)_{Ni}//(031)_{Ni_3B}$ and $(022)_{Ni}//(420)_{Ni_3B}$ by TEM observations. In this work, the aforementioned orientation relationships of $(311)_{Ni}//(420)_{Ni_3B}$, $(111)_{Ni}//(130)_{Ni_3B}$, $(002)_{Ni}//(031)_{Ni_3B}$ and $(022)_{Ni}//(420)_{Ni_3B}$ only have the frequencies of 8.7%, 1.5%, 1.2% and 6.1%, respectively. Correlated the statistical results listed in Table 4 and the IPF maps of Ni_3B and Ni grains (Figs. 7a and 9a), it is reasonably believed that the orientation relationships between the independent Ni_3B colonies and the surrounding Ni grains are varied according to the orientations of the independent Ni_3B colonies. Therefore, only six types of lattice correlation boundaries have the frequencies of over 10%. Meanwhile, it has been reported that the low-lattice-mismatch is in favor of decreasing the strain between the interphase boundaries and reducing the free energy of system [67]. However, the frequencies are considerably low in many types of lattice correlation boundaries between Ni and Ni_3B, although some of them have very low mismatches. Therefore, one can conclude that although specific orientation relationships are presented between the adjacent Ni and Ni_3B grains, the frequencies of lattice correlation boundaries may not completely depend on the lattice mismatches.

In Fig. 13b, four types of lattice correlation boundaries between the adjacent Ni and CrB grains, i.e. $(002)_{Ni}//(040)_{CrB}$, $(311)_{Ni}//(170)_{CrB}$, $(311)_{Ni}//(241)_{CrB}$ and $(311)_{Ni}//(312)_{CrB}$ within 5° tolerance, are also exhibited by red, blue, green and purple lines, respectively. In contrast to the lattice correlation boundaries between the adjacent Ni and Ni_3B grains, the lattice correlation boundary $(002)_{Ni}//(040)_{CrB}$ (red line) has an overwhelming frequency (Fig. 13b). Table 5 shows the lattice mismatches between different couples of the low-index planes of Ni and Ni_3B and the corresponding frequencies of the lattice correlation boundaries. It can be seen that the frequency of the lattice correlation boundary $(311)_{Ni}//(170)_{CrB}$ reaches 40.8%, much higher than those of the other lattice correlation boundaries (Table 5). The lattice correlation boundary with the couple of $(002)_{Ni}//(040)_{CrB}$ has the second-highest relative frequency of 36.7%. The angle between $(311)_{Ni}$ and $(002)_{Ni}$ is 72.5° and the angle between $(170)_{CrB}$ and $(040)_{CrB}$ is 69.3°. Therefore, the blue line and the red line are overlapped in some locations. It also should be noted that the mismatches are 0.014 between $(311)_{Ni}$ and $(170)_{CrB}$ and 0.1 between $(002)_{Ni}$ and $(040)_{CrB}$, much larger than the other couples of the planes of Ni and CrB listed in Table 5. This confirms again that the formation of the lattice correlation boundaries is not absolutely dependent on the lattice mismatches. Overall, such a result gives a factor that the orientations of the CrB and Ni grains strongly interact with each other.

Table 6 lists the lattice mismatches between different couples of the low-index planes of Ni_3B and CrB and the corresponding frequencies of the lattice correlation boundaries. All examined lattice correlation boundaries have extremely low frequencies. The highest frequency of lattice correlation boundary $(102)_{Ni_3B}//(111)_{CrB}$ is 5.93%. According to the texture components of Ni_3B and CrB in Figs. 8 and 10, the different couples of planes with the comparable mismatch between the (012), (021) planes of Ni_3B and (010), (212) and (170) planes of CrB are also examined. The frequencies of lattice correlation boundaries with these couples of planes are still very low. As mentioned in Section 3.2, most CrB grains are embedded in or adjacent to the Ni grains, but not in or

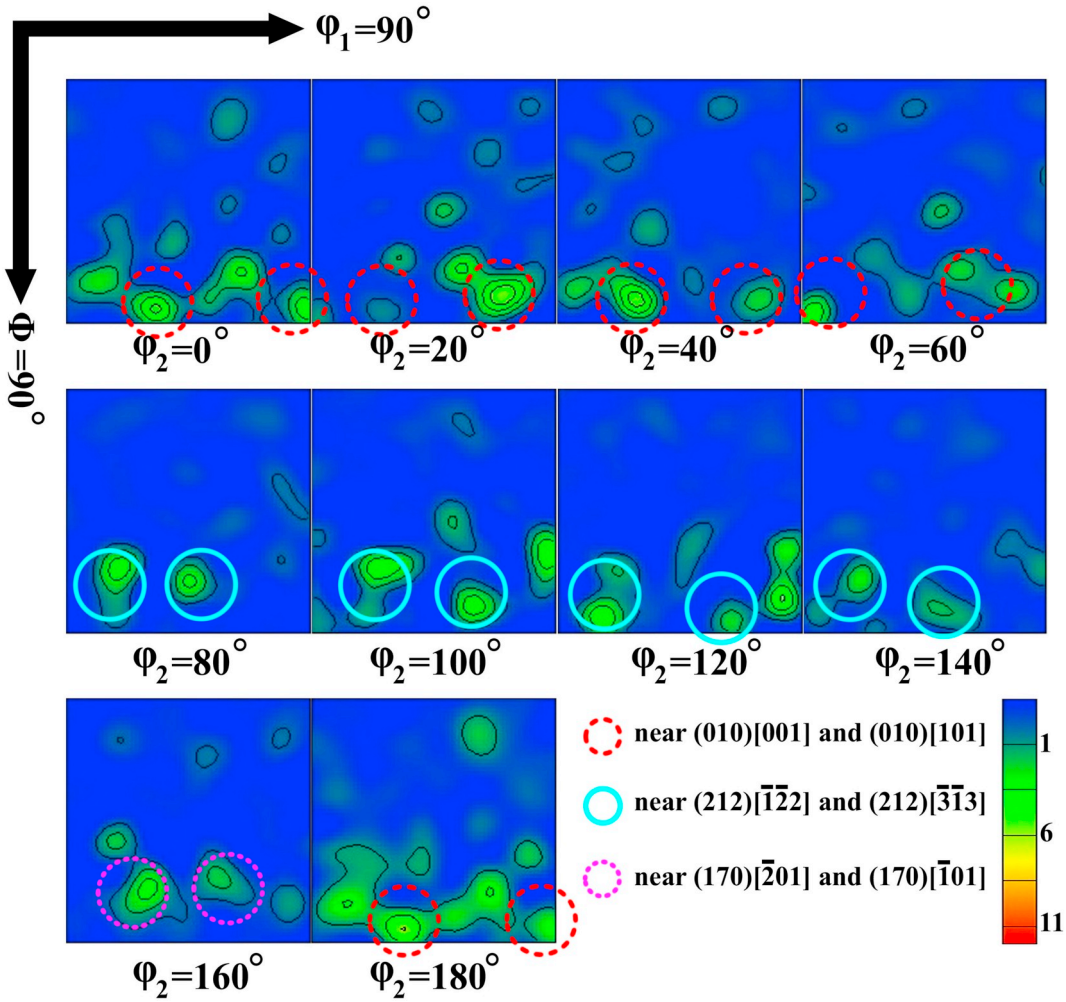

Fig. 12. Selected orientation distribution functions of the CrB grains in the remelted NiCrBSi coating.

adjacent to the Ni_3B grains (Fig. 5). These results indicate that almost no specific orientation relationships are presented between the adjacent Ni_3B and CrB grains.

4. Discussion

Due to the limitation of APS technology, pores and lamellar structures are presented in the as-sprayed NiCrBSi coatings. Therefore, the remelting process is employed to improve the properties of the as-sprayed coatings. However, a further improvement of the remelted NiCrBSi coatings is rarely reported, impeding their wider applications. Meanwhile, considering the existence of a large number of low-symmetry structural precipitates (i.e. Ni_3B and CrB), it is reasonable to believe that the orientations of these precipitates would play a prominent role in the properties of the NiCrBSi coatings. Hence, to better understand the texture of the remelted NiCrBSi coatings may be a potential way to further enhance their properties. As the NiCrBSi alloy has a multiphase microstructure, the formation of the texture is a result of the interaction between the precipitates. Especially, the precipitates have distinctive melting points, thereby they would precipitate from the liquid during the solidification of the remelted NiCrBSi coating. As such, in this work, a detailed EBSD characterization is conducted to investigate the phase interaction induced texture in a plasma sprayed-remelted NiCrBSi coating during solidification.

In this work, Ni, Ni_3B and CrB phases are considered for simplicity since these three phases are commonly observed in the NiCrBSi alloys in the literature [1,2,9]. The influence of Si on the solidification is ignored because the Si does not affect the solidification sequence of Ni, Ni_3B and CrB [30,68]. In previous studies, the ternary phase diagram of Ni-Cr-B has been systematically investigated [40,41]. Therefore, according to the ternary phase diagram of Ni-Cr-B, it could be well known that the as-sprayed NiCrBSi coating is melted during the remelting process because the elevated temperature (over 1500 °C) is higher than the melting point of the NiCrBSi alloys. Therefore, the cooling of the remelted NiCrBSi coating could be regarded as a solidification at a relatively slow rate. Based on the results mentioned above, the formation of the texture associated with the solidification sequence of Ni, Ni_3B and CrB in the remelted NiCrBSi coating could be further understood.

It is well known that the Ni-rich FCC solid solution as the primary phase firstly forms at about 1100 °C [40]. The Ni crystallites nucleate as nodules or simply grow onto the other Ni crystallites within the melt [68]. As reported in the literature [63,64,69], the cube fiber is a typical recrystallized texture and always found in as-cast and recrystallized Ni-based alloys, which is similar to the scenario in this work. Therefore, as observed in Fig. 8, the remelted NiCrBSi coating has a strong cube texture component. On further cooling, the formation of a binary eutectic of Ni and Ni_3B commences at about 1042 °C [40,68]. It should be noted that the orientations among independent Ni_3B colonies are basically random, indicating the random appearance of Ni_3B nuclei in the melt (Fig. 9a). There are different colored Ni grains surrounding each Ni_3B colony (Figs. 7a and 9a), implying that the orientations of these Ni grains seem to be random. However, the investigation of lattice correlation boundaries shows that the specific orientation relationships between the Ni_3B colonies and their surrounding Ni grains are presented

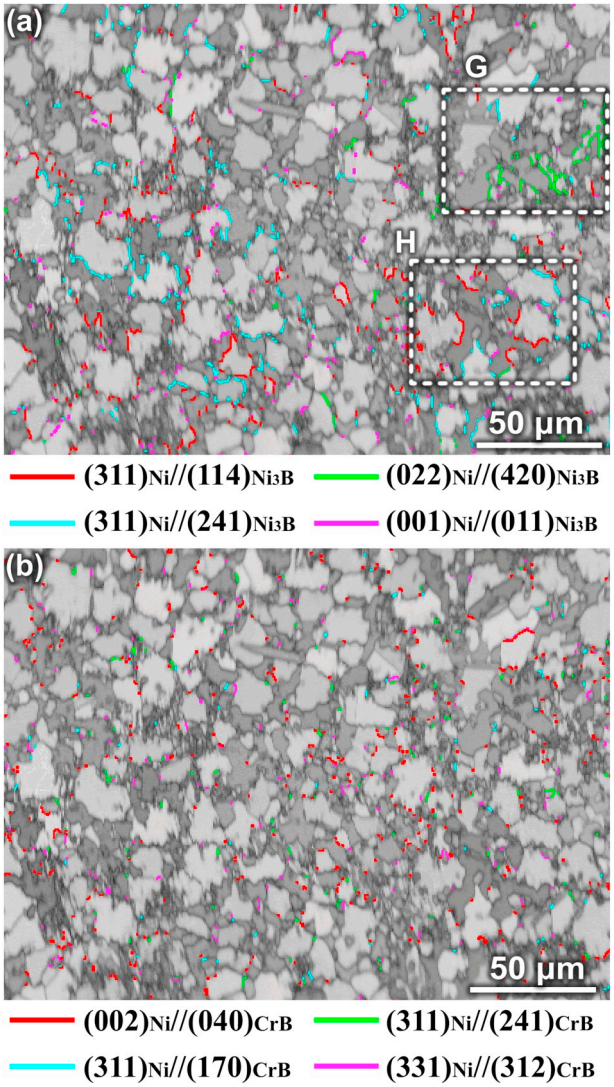

Fig. 13. Selected lattice correlation boundaries represented by different colors: (a) between the adjacent Ni and Ni_3B grains, (b) between the adjacent Ni and CrB grains. The dash rectangles G and H in (a) contain two independent Ni_3B colonies.

(Fig. 13a and Table 4). Therefore, it illustrates that the surrounding Ni grains are not in the fully random orientations, which are interacted by the formed Ni_3B colony and keep the specific orientation relationships with them. This phenomenon could outline the formation of Ni and Ni_3B by the eutectic reaction. After the firstly formed Ni grains, the eutectic reaction of Ni and Ni_3B takes place. As reported in the literature [31], the eutectic grains would keep specific orientation relationships in order to reduce the interfacial energy. Hence, one can observe the specific orientation relationships between the Ni_3B colonies and their surrounding Ni grains (Fig. 13a and Table 4). Therefore, under the interaction of the Ni_3B colonies, some other weak texture components of Ni grains are induced besides the cube fiber texture (Fig. 7). Meanwhile, not all Ni grains keep specific orientation relationships with the surrounded Ni_3B colonies (Fig. 13a). It is speculated that some Ni grains may have a small rotation or floating in the remnant liquid [31]. Hence, based on the result of lattice correlation boundaries of Ni and Ni_3B grains in Table 4, one could conclude that the interaction of the Ni and Ni_3B grains is not strong.

As such, the formation of the eutectic of Ni and Ni_3B enriches the remaining melt with Cr. Meanwhile, it has been reported that a large amount of Cr is in solid solution in the Ni and Ni_3B grains [30,70]. As the temperature decreases, a ternary eutectic of Ni, Ni_3B and CrB takes place at about 997 °C [68]. Along with the formation of CrB grains from the melt, the Cr atoms are also rejected from the Ni and Ni_3B grains due to the reduction of the temperature, promoting the production of more CrB grains [65]. By carefully comparing the ODFs of Ni and CrB in Figs. 8 and 12, one can find that the Ni grains have the major texture components of $\{001\}\langle 100\rangle$ and near $\{311\}\langle 2\bar{5}1\rangle$ and $\{331\}\langle 0\bar{1}3\rangle$ and the CrB grains have the major texture components near (010)[001], (010)[101], $(212)[\bar{1}\bar{2}2]$, $(212)[\bar{3}\bar{1}3]$, (170)[302] and (170)[203]. The corresponding lattice correlation boundaries $(311)_{Ni}//(170)_{CrB}$ and $(002)_{Ni}//(040)_{CrB}$ have very high frequencies of 36.7% and 40.8% (Table 5). The lattice correlation boundary $(331)_{Ni}//(312)_{CrB}$ also has a relatively high frequency of 12.5% (Table 5). It is noted that the (212) plane of CrB is approximately to perpendicular to the direction Z of the sample in the texture components of $(212)[\bar{1}\bar{2}2]$ and $(212)[\bar{3}\bar{1}3]$ and the angle between the planes of (212) and (312) of CrB is merely 11.4°. Considering the basic error of ODFs and the tolerance of the lattice correlation boundary, it could believe that the plane of (212) of CrB is only tilted by a very small angle to the plane of (331) of Ni at the lattice correlation boundary $(331)_{Ni}//(312)_{CrB}$. Therefore, one can confirm that the orientations of CrB and Ni grains significantly interact with each other, which results in the rotation of the CrB and Ni grains during solidification. Hence, more texture components of Ni grains are induced besides the cube fiber and the CrB grains show apparent orientations. As aforementioned that almost no specific orientation relationships are presented between the adjacent Ni_3B and CrB grains (Table 6) and most CrB grains are embedded in or adjacent to the Ni grains but not in or adjacent to Ni_3B grains (Fig. 5), it is rationally speculated that most Cr atoms in CrB grains come from the melt or the solid solution in Ni grains. Hence there should be still a large amount of Cr atom in solid solution in the Ni_3B grains. Such a deduction is consistent with the result proposed by Siredey et al. [30] that the Ni_3B grains contain about 8 wt% Cr in solid solution at room temperature in terms of the composition of the feedstock used in this work. Table 3 shows that there are about 29.6 vol% Ni_3B grains in substructured after complete solidification. Hence, such a high-volume fraction of substructured Ni_3B grains might result from the lattice strain and defect induced by Cr solid solution in Ni_3B. Therefore, it could understand that the last formation of CrB grains strongly interact with the Ni grains but not Ni_3B grains.

Based on above discussion, it is noted that due to a wide temperature range of solidification, although the firstly formed Ni grains have a cube fiber texture, the subsequently formed Ni_3B and CrB grains strongly interact with the Ni grains in the form of the related specific orientations, which results in various texture components of Ni, Ni_3B and CrB grains in the remelted NiCrBSi coating. Therefore, these results demonstrate that the texture in the remelted NiCrBSi coating is induced by phase interaction. For the coatings reinforced by hard phases, the hardness and the wear resistance of the coatings could be improved if the close-arranged planes of the hard phases are parallel to the surface of the coatings [27]. Therefore, some simple methods can be considered to control the texture. For example, the samples placed with an angle tilted from the vertical plane during spraying and remelting process can control the texture of the remelting NiCrBSi coatings. As solidification process is a function of the cooling rate, different agents may result in different textures in the coatings and thereby further influence the properties of the remelted NiCrBSi coatings. Some other simple methods, such as backward and forward scanning of plasma torch [71] or applying a strong magnetic field during the remelting process [72], can also be considered. Even more, as the additions of Ni_3B and CrB phases play a role in improving the hardness and wear resistance of the NiCrBSi coatings, designing the volume fractions of these phases could tailor intensity of the texture in the remelted NiCrBSi coating and enhance its properties. Therefore, it could be concluded that this work provides a theoretical basis for further tailoring the microstructure of the remelted NiCrBSi coating.

Table 4
Summary of the lattice mismatches between different couples of the low-index planes of Ni and Ni_3B and the corresponding frequencies of the lattice correlation boundaries.

Ni		Ni_3B		Mismatch	Frequency (%)
Plane	Spacing (nm)	Plane	Spacing (nm)		
(311)	0.1065	(114)	0.1061	0.004	16.15%
(111)	0.2040	(220)	0.2048	0.004	2.60%
(111)	0.2040	(102)	0.2025	0.007	1.50%
(311)	0.1065	(431)	0.1087	0.020	14.69%
(011)	0.2498	(210)	0.2423	0.030	6.10%
(311)	0.1065	(004)	0.1098	0.030	4.00%
(022)	0.1249	(420)	0.1211	0.030	6.10%
(311)	0.1065	(060)	0.1103	0.034	5.00%
(001)	0.3534	(011)	0.3662	0.035	11.10%
(011)	0.2498	(200)	0.2605	0.041	11.90%
(002)	0.1767	(131)	0.1844	0.042	3.90%
(001)	0.3534	(101)	0.3358	0.050	3.30%
(022)	0.1249	(042)	0.1322	0.055	13.00%
(002)	0.1767	(031)	0.1971	0.104	1.20%
(311)	0.1065	(420)	0.1210	0.120	8.70%
(002)	0.1767	(012)	0.2086	0.153	1.77%
(311)	0.1065	(241)	0.1331	0.200	17.50%

Table 5
Summary of the lattice mismatches between different couples of the low-index planes of Ni and CrB and the corresponding frequencies of the lattice correlation boundaries.

Ni		CrB		Mismatch	Frequency (%)
Plane	Spacing (nm)	Plane	Spacing (nm)		
(400)	0.0883	(331)	0.0882	0.001	3.13%
(022)	0.1249	(151)	0.1255	0.005	7.90%
(022)	0.1249	(221)	0.1255	0.005	6.20%
(331)	0.0811	(262)	0.0815	0.005	9.30%
(331)	0.0811	(312)	0.0815	0.005	12.50%
(400)	0.0883	(043)	0.0875	0.009	1.30%
(400)	0.0883	(133)	0.0875	0.009	2.90%
(331)	0.0811	(280)	0.0819	0.010	6.50%
(111)	0.2040	(111)	0.2016	0.012	4.30%
(311)	0.1065	(170)	0.1050	0.014	40.80%
(311)	0.1065	(202)	0.1043	0.021	5.80%
(311)	0.1065	(212)	0.1034	0.029	9.21%
(311)	0.1065	(241)	0.1098	0.030	10.40%
(111)	0.2040	(040)	0.1964	0.037	1.20%
(011)	0.2498	(021)	0.2349	0.060	2.80%
(002)	0.1767	(131)	0.1631	0.077	4.20%
(002)	0.1767	(041)	0.1631	0.077	1.20%
(002)	0.1767	(130)	0.1964	0.100	2.30%
(002)	0.1767	(040)	0.1964	0.100	36.70%
(011)	0.2498	(110)	0.2777	0.100	6.00%
(331)	0.0811	(212)	0.1034	0.216	13.49%

Table 6
Summary of the lattice mismatches between different couples of the low-index planes of Ni_3B and CrB and the corresponding frequencies of the lattice correlation boundaries.

Ni_3B		CrB		Mismatch	Frequency (%)
Plane	Spacing (nm)	Plane	Spacing (nm)		
(004)	0.1098	(241)	0.1098	0.000	0.89%
(031)	0.1971	(040)	0.1964	0.004	0.89%
(031)	0.1971	(130)	0.1964	0.004	2.77%
(102)	0.2025	(111)	0.2016	0.004	5.93%
(060)	0.1103	(241)	0.1098	0.005	1.09%
(220)	0.2048	(111)	0.2016	0.016	2.67%
(102)	0.2025	(130)	0.1964	0.030	1.58%
(210)	0.2423	(021)	0.2349	0.031	1.48%
(420)	0.1211	(151)	0.1255	0.035	3.07%
(420)	0.1211	(221)	0.1255	0.035	2.87%
(220)	0.2048	(040)	0.1964	0.041	0.79%
(004)	0.1098	(170)	0.1050	0.044	2.47%
(004)	0.1098	(202)	0.1043	0.050	0.69%
(042)	0.1322	(221)	0.1255	0.051	3.26%
(241)	0.1331	(221)	0.1255	0.057	2.37%
(200)	0.2605	(110)	0.2777	0.062	0.30%
(011)	0.3662	(020)	0.3929	0.068	0.99%
(131)	0.1844	(131)	0.1631	0.116	3.17%
(131)	0.1844	(041)	0.1631	0.116	2.97%
(021)	0.2350	(040)	0.1964	0.164	0.30%
(012)	0.1441	(170)	0.1050	0.271	1.38%
(012)	0.1441	(212)	0.1034	0.282	3.56%

5. Conclusions

In this work, a plasma sprayed-remelted NiCrBSi coating was examined by electron backscatter diffraction (EBSD). As the Ni, Ni_3B and CrB are the primary phases in the remelted NiCrBSi coating, these three phases are selected to for the EBSD characterization. Grain size, recrystallized fraction, orientation for each phase and the lattice correlation boundaries between these phases are investigated. The texture formation of the remelted NiCrBSi coating is discussed based on the solidification sequence of Ni, Ni_3B and CrB. Some key conclusions can be drawn as follows:

(1) The Ni, Ni_3B and CrB grains are uniformly distributed in the remelted coating and their volume fractions are 59.6%, 24.6% and 5.7%, respectively. The average grain sizes for Ni, Ni_3B and CrB are 5.2 μm, 1.9 μm and 1.1 μm respectively. Both Ni and CrB grains have very high recrystallized fractions of 93.6% and 91.7% respectively, whereas the recrystallized fraction of Ni_3B grains is only 68.4%. Correspondingly, the substructured fraction of Ni_3B grains reaches 29.6%.

(2) The Ni grains have a strong cube fiber texture of {001}⟨001⟩ and three other texture components of (137)[137], (311)[251] and (331)[$0\bar{1}3$] with slightly weak intensities. Furthermore, some other texture components of (221)[$2\bar{4}3$] and (312)[$1\bar{2}3$] with very weak intensities could be found for the Ni grains. The orientations of the Ni_3B grains are primarily random that mainly consist of four texture components of (012)[$0\bar{1}1$], (431)[211], (021)[$0\bar{1}2$] and (114)[$\bar{3}\bar{1}0$]. The following three strong texture components observed in CrB grains are (010)[001] and (010)[101], (212)[$\bar{1}\bar{2}2$] and (212)[$\bar{3}\bar{1}3$], (170)[302] and (170)[203]. The texture components presented in pairs may be related to the highly resided twins in CrB grains.

(3) The specific orientation relationships are found between the independent Ni_3B colonies and surrounding Ni grains, which are varied depending on the orientations of the independent Ni_3B colonies. Only six types of lattice correlation boundaries have the frequencies of more than 10%. The frequencies of the lattice correlation boundaries $(311)_{Ni}//(170)_{CrB}$ and $(002)_{Ni}//(040)_{CrB}$ are 40.8% and 36.7% respectively, which are overwhelmingly higher than those of the other lattice correlation boundaries. This indicates that the orientations of the Ni and CrB grains strongly interact with each other. However, almost no specific orientation relationships are presented between the adjacent Ni_3B and CrB grains.

(4) By correlating the solidification sequence of Ni, Ni_3B and CrB in the remelted NiCrBSi coating during cooling, it is suggested that the cube fiber texture is produced in the firstly formed Ni grains. The Ni_3B grains form subsequently. Due to the specific orientation relationships between the Ni_3B grains and surrounding Ni grains, some other weak texture components of Ni grains form. The CrB grains form at last. Associated with the fact that the orientations of CrB and Ni grains significantly interact with each other, more texture components of Ni grains form. Therefore, it demonstrates that the phase interaction takes place during solidification and the resultant texture in the remelted NiCrBSi coating.

Acknowledgment

The authors would like to acknowledge a financial support provided by National Natural Science Foundation of China (51601075 and 51375218), China Postdoctoral Science Foundation Funded Project (2017M611751), Postgraduate Research & Practice Innovation Program of Jiangsu Province, and Jiangsu University of Science and Technology Overseas Research & Training Program for University Prominent Young & Middle-aged Teachers.

Declarations of interest

None.

References

[1] C. Shi, J. Lei, S. Zhou, X. Dai, L.C. Zhang, Microstructure and mechanical properties of carbon fibers strengthened Ni-based coatings by laser cladding: the effect of carbon fiber contents, J. Alloys Compd. 744 (2018) 146–155.
[2] J. Lei, C. Shi, S. Zhou, Z. Gu, L.C. Zhang, Enhanced corrosion and wear resistance properties of carbon fiber reinforced Ni-based composite coating by laser cladding, Surf. Coat. Technol. 334 (2018) 274–285.
[3] L.-Y. Chen, T. Xu, S. Lu, Z.-X. Wang, S. Chen, L.-C. Zhang, Improved hardness and wear resistance of plasma sprayed nanostructured NiCrBSi coating via short-time heat treatment, Surf. Coat. Technol. 350 (2018) 436–444.
[4] Y. Li, T. Dong, G. Li, H. Wang, B. Fu, X. Zheng, Microstructure evolution and properties of NiCrBSi thick coating remelted by gas tungsten arc, Surf. Coat. Technol. 349 (2018) 260–271.
[5] J. Chen, Y. Dong, L. Wan, Y. Yang, Z. Chu, J. Zhang, J. He, D. Li, Effect of induction remelting on the microstructure and properties of in situ TiN-reinforced NiCrBSi composite coatings, Surf. Coat. Technol. 340 (2018) 159–166.
[6] A. Salimi, S. Sanjabi, Infiltration brazed core-shell WC@NiP/NiCrBSi composite cladding, Surf. Coat. Technol. 352 (2018) 59–73.
[7] L. Wang, L. Xie, L.C. Zhang, L. Chen, Z. Ding, Y. Lv, W. Zhang, W. Lu, D. Zhang, Microstructure evolution and superelasticity of layer-like NiTiNb porous metal prepared by eutectic reaction, Acta Mater. 143 (2018) 214–226.
[8] Š. Houdková, E. Smazalová, M. Vostřák, J. Schubert, Properties of NiCrBSi coating, as sprayed and remelted by different technologies, Surf. Coat. Technol. 253 (2014) 14–26.
[9] Z. Chang, W. Wang, Y. Ge, J. Zhou, Z. Cui, Microstructure and mechanical properties of Ni-Cr-Si-B-Fe composite coating fabricated through laser additive manufacturing, J. Alloys Compd. 747 (2018) 401–407.
[10] J. Sun, J. Wang, S. Dong, Y. Hui, L. Li, L. Deng, J. Jiang, X. Zhou, X. Cao, Effect of heat treatment on microstructure and property of plasma-sprayed lanthanum hexaaluminate coating, J. Alloys Compd. 739 (2018) 856–865.
[11] C. Navas, R. Colaço, J. de Damborenea, R. Vilar, Abrasive wear behaviour of laser clad and flame sprayed-melted NiCrBSi coatings, Surf. Coat. Technol. 200 (2006) 6854–6862.
[12] W. Żórawski, S.J. Skrzypek, Tribological properties of plasma and HVOF-sprayed NiCrBSi–Fe_2O_3 composite coatings, Surf. Coat. Technol. 220 (2013) 282–289.
[13] H. Singh, B.S. Sidhu, D. Puri, S. Prakash, Use of plasma spray technology for deposition of high temperature oxidation/corrosion resistant coatings - a review, Mater. Corros. 58 (2007) 92–102.
[14] P. Niranatlumpong, H. Koiprasert, Phase transformation of NiCrBSi-WC and NiBSi-WC arc sprayed coatings, Surf. Coat. Technol. 206 (2011) 440–445.
[15] L. Liu, H. Xu, J. Xiao, X. Wei, G. Zhang, C. Zhang, Effect of heat treatment on structure and property evolutions of atmospheric plasma sprayed NiCrBSi coatings, Surf. Coat. Technol. 325 (2017) 548–554.
[16] Z. Bergant, U. Trdan, J. Grum, Effect of high-temperature furnace treatment on the microstructure and corrosion behavior of NiCrBSi flame-sprayed coatings, Corros. Sci. 88 (2014) 372–386.
[17] S. Hong, Y. Wu, G. Li, B. Wang, W. Gao, G. Ying, Microstructural characteristics of high-velocity oxygen-fuel (HVOF) sprayed nickel-based alloy coating, J. Alloys Compd. 581 (2013) 398–403.
[18] X.C. Yang, G.L. Li, H.D. Wang, T.S. Dong, J.J. Kang, Effect of flame remelting on microstructure and wear behaviour of plasma sprayed NiCrBSi-30%Mo coating, Surf. Eng. 34 (2018) 181–188.
[19] D. Kong, B. Zhao, Effects of loads on friction–wear properties of HVOF sprayed NiCrBSi alloy coatings by laser remelting, J. Alloys Compd. 705 (2017) 700–707.
[20] D.Z. Guo, F.L. Li, J.Y. Wang, J.S. Sun, Effects of post-coating processing on structure and erosive wear characteristics of flame and plasma spray coatings, Surf. Coat. Technol. 73 (1995) 73–76.
[21] N. Serres, F. Hlawka, S. Costil, C. Langlade, F. MacHi, Microstructures of metallic NiCrBSi coatings manufactured via hybrid plasma spray and in situ laser remelting process, J. Therm. Spray Technol. 20 (2011) 336–343.
[22] I. Hemmati, J.C. Rao, V. Ocelik, J.T.M. De Hosson, Electron microscopy characterization of Ni-Cr-B-Si-C laser deposited coatings, Microsc. Microanal. 19 (2013) 120–131.
[23] T. Gómez-del Río, M.A. Garrido, J.E. Fernández, M. Cadenas, J. Rodríguez, Influence of the deposition techniques on the mechanical properties and microstructure of NiCrBSi coatings, J. Mater. Process. Technol. 204 (2008) 304–312.
[24] Z. Bergant, J. Grum, Quality improvement of flame sprayed, heat treated, and Remelted NiCrBSi coatings, J. Therm. Spray Technol. 18 (2009) 380–391.
[25] X. Li, J. Deng, L. Liu, L. Zhang, J. Sun, D. Ge, Y. Liu, R. Duan, Tribological properties of WS2 coatings deposited on textured surfaces by electrohydrodynamic atomization, Surf. Coat. Technol. 352 (2018) 128–143.
[26] N. Jantaping, C.A. Schuh, Y. Boonyongmaneerat, Influences of crystallographic texture and nanostructural features on corrosion properties of electrogalvanized and chromate conversion coatings, Surf. Coat. Technol. 329 (2017) 120–130.
[27] H.S. Maharana, S. Panda, A. Basu, Effect of texture and microstructure on properties of electrodeposited Cu-$SiO_2$and Cu-Y_2O_3 coatings, Surf. Coat. Technol. 315 (2017) 558–566.
[28] N. Dai, J. Zhang, Y. Chen, L.-C. Zhang, Heat treatment degrading the corrosion resistance of selective laser melted Ti-6Al-4V alloy, J. Electrochem. Soc. 164 (2017) C428–C434.
[29] D. Zhang, F. Gao, X. Wei, G. Liu, M. Hua, P. Li, Fabrication of textured composite surface and its tribological properties under starved lubrication and dry sliding conditions, Surf. Coat. Technol. 350 (2018) 313–322.
[30] N. Siredey-Schwaller, J. Hamel-Akré, L. Peltier, A. Hazotte, P. Bocher, Solidification sequence of Ni-Si-Cr ~3wt% B brazing alloys, Weld. World 61 (2017) 1253–1265.
[31] M. Li, K. Nagashio, T. Ishikawa, S. Yoda, K. Kuribayashi, Microtexture and macrotexture formation in the containerless solidification of undercooled Ni-18.7 at.% Sn eutectic melts, Acta Mater. 53 (2005) 731–741.
[32] L. Chai, K. Chen, Y. Zhi, K.L. Murty, L.Y. Chen, Z. Yang, Nanotwins induced by pulsed laser and their hardening effect in a Zr alloy, J. Alloys Compd. 748 (2018) 163–170.
[33] L.J. Chai, S.Y. Wang, H. Wu, N. Guo, H.C. Pan, L.Y. Chen, K.L. Murty, B. Song, α→β Transformation characteristics revealed by pulsed laser-induced non-equilibrium microstructures in duplex-phase Zr alloy, Sci. China Technol. Sci. 60 (2017) 1255–1262.
[34] J. Qiao, L. Zhu, W. Yue, Z. Fu, J. Kang, C. Wang, The effect of attributes of micro-shapes of laser surface texture on the wettability of WC-CrCo metal ceramic coatings, Surf. Coat. Technol. 334 (2018) 429–437.
[35] C. Tang, K. Wu, W. Liu, D. Feng, X. Wang, G. Miao, M. Yang, X. Liu, Q. Li, Effects of Gd, Y content on the microstructure and mechanical properties of Mg-Gd-Y-Nd-Zr alloy, Metals 8 (2018) 790.
[36] L. Chen, J. Li, Y. Zhang, W. Lu, L.C. Zhang, L. Wang, D. Zhang, Effect of low-temperature pre-deformation on precipitation behavior and microstructure of a Zr-Sn-Nb-Fe-Cu-O alloy during fabrication, J. Nucl. Sci. Technol. 53 (2016) 496–507.
[37] L. Chen, Q. Zeng, J. Li, J. Lu, Y. Zhang, L.-C. Zhang, X. Qin, W. Lu, L. Zhang, L. Wang, D. Zhang, Effect of microstructure on corrosion behavior of a Zr–Sn–Nb–Fe–Cu–O alloy, Mater. Des. 92 (2016) 888–896.
[38] L.-C. Zhang, Y. Liu, S. Li, Y. Hao, Additive manufacturing of titanium alloys by Electron beam melting: a review, Adv. Eng. Mater. 20 (2018) 1700842.
[39] J. Liu, R. Bolot, S. Costil, M.P. Planche, Transient thermal and mechanical analysis of NiCrBSi coatings manufactured by hybrid plasma spray process with in-situ laser remelting, Surf. Coat. Technol. 292 (2016) 132–143.
[40] K. Ohsasa, T. Shinmura, T. Narita, Numerical modeling of the transient liquid phase bonding process of Ni using Ni-B-Cr ternary filler metal, J. Phase Equilib. 20 (1999) 199–206.
[41] C.E. Campbell, U.R. Kattner, Assessment of the Cr-B system and extrapolation to the Ni-Al-Cr-B quaternary system, Calphad 26 (2002) 477–490.
[42] S. Lebaili, M. Durand-Charre, S. Hamar-Thibault, The metallurgical structure of as-solidified Ni-Cr-B-Si-C hardfacing alloys, J. Mater. Sci. 23 (1988) 3603–3611.
[43] M. Liu, G. Sheng, H. He, Y. Jiao, Microstructural evolution and mechanical properties of TLP bonded joints of mar-M247 superalloys with Ni-Cr-Co-W-Ta-B interlayer, J. Mater. Process. Technol. 246 (2017) 245–251.
[44] H. Gleiter, On the structure of grain boundaries m metals, Interfacial Asp. Phase Transform. Springer, 1982, pp. 91–131.
[45] T. Schober, R.W. Balluffi, Quantitative observation of misfit dislocation arrays in low and high angle twist grain boundaries, Philos. Mag. 21 (1970) 109–123.
[46] P.H. Pumphrey, H. Gleiter, On the structure of non-equilibrium high-angle grain boundaries, Philos. Mag. 32 (1975) 881–885.
[47] F.J. Humphreys, Grain and subgrain characterisation by electron backscatter diffraction, J. Mater. Sci. 36 (2001) 3833–3854.
[48] H.J. Bunge, Three-dimensional texture analysis, Int. Mater. Rev. 32 (1987) 265–291.
[49] G. Cacciamani, A. Dinsdale, M. Palumbo, A. Pasturel, The Fe-Ni system: thermodynamic modelling assisted by atomistic calculations, Intermetallics 18 (2010) 1148–1162.
[50] S. Dong, B. Song, H. Liao, C. Coddet, Deposition of NiCrBSi coatings by atmospheric plasma spraying and dry-ice blasting: microstructure and wear resistance, Surf. Coat. Technol. 268 (2015) 36–45.
[51] L.C. Zhang, J. Xu, Glass-forming ability of melt-spun multicomponent (Ti, Zr, Hf)-(Cu, Ni, Co)-Al alloys with equiatomic substitution, J. Non-Cryst. Solids 347 (2004) 166–172.
[52] L.C. Zhang, J. Xu, E. Ma, Mechanically alloyed amorphous $Ti_{50}(Cu_{0.45}Ni_{0.55})_{44-x}Al_xSi_4B_2$ alloys with supercooled liquid region, J. Mater. Res. 17 (2002) 1743–1749.
[53] L.C. Zhang, K.B. Kim, P. Yu, W.Y. Zhang, U. Kunz, J. Eckert, Amorphization in mechanically alloyed (Ti, Zr, Nb)–(Cu, Ni)–Al equiatomic alloys, J. Alloys Compd. 428 (2007) 157–163.
[54] L.C. Zhang, Z.Q. Shen, J. Xu, Mechanically milling-induced amorphization in Sn-containing Ti-based multicomponent alloy systems, Mater. Sci. Eng. A 394 (2005) 204–209.
[55] S.-X. Liang, Z. Jia, Y.-J. Liu, W. Zhang, W. Wang, J. Lu, L.-C. Zhang, Compelling rejuvenated catalytic performance in metallic glasses, Adv. Mater. 30 (2018)

1802764.
[56] S.X. Liang, Z. Jia, W.C. Zhang, W.M. Wang, L.C. Zhang, Rapid malachite green degradation using $Fe_{73.5}Si_{13.5}B_9Cu_1Nb_3$ metallic glass for activation of persulfate under UV–Vis light, Mater. Des. 119 (2017) 244–253.
[57] Y. Zou, W. Qin, E. Irissou, J.G. Legoux, S. Yue, J.A. Szpunar, Dynamic recrystallization in the particle/particle interfacial region of cold-sprayed nickel coating: Electron backscatter diffraction characterization, Scr. Mater. 61 (2009) 899–902.
[58] M. Calin, L.C. Zhang, J. Eckert, Tailoring of microstructure and mechanical properties of a Ti-based bulk metallic glass-forming alloy, Scr. Mater. 57 (2007) 1101–1104.
[59] C.D. Rabadia, Y.J. Liu, L. Wang, H. Sun, L.C. Zhang, Laves phase precipitation in Ti-Zr-Fe-Cr alloys with high strength and large plasticity, Mater. Des. 154 (2018) 228–238.
[60] K. Shinoda, M. Demura, H. Murakami, S. Kuroda, S. Sampath, Characterization of crystallographic texture in plasma-sprayed splats by electron-backscattered diffraction, Surf. Coat. Technol. 204 (2010) 3614–3618.
[61] X.M. Chen, Y.C. Lin, F. Wu, EBSD study of grain growth behavior and annealing twin evolution after full recrystallization in a nickel-based superalloy, J. Alloys Compd. 724 (2017) 198–207.
[62] N.R. Tao, X.L. Wu, M.L. Sui, J. Lu, K. Lu, Grain refinement at the nanoscale via mechanical twinning and dislocation interaction in a nickel-based alloy, J. Mater. Res. 19 (2004) 1623–1629.
[63] P.P. Bhattacharjee, R.K. Ray, N. Tsuji, Cold rolling and recrystallization textures of a Ni-5 at.% W alloy, Acta Mater. 57 (2009) 2166–2179.
[64] S.M. Seo, I.S. Kim, J.H. Lee, C.Y. Jo, H. Miyahara, K. Ogi, Grain structure and texture evolutions during single crystal casting of the Ni-Base superalloy CMSX-4, Met. Mater. Int. 15 (2009) 391–398.
[65] J.A. Ajao, Phase transitions in some nickel-rich nickel-boron-titanium hard alloys, J. Alloys Compd. 493 (2010) 314–321.
[66] S. Shapiro, J.A. Ford, Crystallography of unidirectionally solidified Ni-Ni_3B eutectic alloy, Trans. Metall. Soc. AIME 236 (1966) 536–542.
[67] Y. Chen, J. Washburn, Structural transition in large-lattice-mismatch heteroepitaxy, Phys. Rev. Lett. 77 (1996) 19–22.
[68] S.K. Tung, L.C. Lim, M.O. Lai, Solidification phenomena in nickel base brazes containing boron and silicon, Scr. Mater. 34 (1996) 763–769.
[69] M.G. Ardakani, N. D'Souza, B.A. Shollock, M. McLean, Directional and single-crystal solidification of Ni-base superalloys: Part II. Coincidence site lattice character of grain boundaries, Metall. Mater. Trans. A Phys. Metall. Mater. Sci. 31 (2000) 2887–2893.
[70] B.P. Nash, The Cr-Ni (chromium-nickel) system, Bull. Alloy Phase Diagr. 7 (1986) 466–476.
[71] G.P. Dinda, A.K. Dasgupta, J. Mazumder, Texture control during laser deposition of nickel-based superalloy, Scr. Mater. 67 (2012) 503–506.
[72] T.S. Suzuki, T. Uchikoshi, Y. Sakka, Control of texture in alumina by colloidal processing in a strong magnetic field, Sci. Technol. Adv. Mater. 7 (2006) 356–364.